Empirical conversion of the vertical profile of reflectivity from Ku-band to S-band frequency

Qing Cao,[1,2] Yang Hong,[1,2,3] Youcun Qi,[4] Yixin Wen,[1,2] Jian Zhang,[4] Jonathan J. Gourley,[4] and Liang Liao[5]

Received 3 October 2012; revised 17 December 2012; accepted 18 December 2012; published 25 February 2013.

[1] This paper presents an empirical method for converting reflectivity from Ku-band (13.8 GHz) to S-band (2.8 GHz) for several hydrometeor species, which facilitates the incorporation of Tropical Rainfall Measuring Mission (TRMM) Precipitation Radar (PR) measurements into quantitative precipitation estimation (QPE) products from the U.S. Next-Generation Radar (NEXRAD). The development of empirical dual-frequency relations is based on theoretical simulations, which have assumed appropriate scattering and microphysical models for liquid and solid hydrometeors (raindrops, snow, and ice/hail). Particle phase, shape, orientation, and density (especially for snow particles) have been considered in applying the T-matrix method to compute the scattering amplitudes. Gamma particle size distribution (PSD) is utilized to model the microphysical properties in the ice region, melting layer, and raining region of precipitating clouds. The variability of PSD parameters is considered to study the characteristics of dual-frequency reflectivity, especially the variations in radar dual-frequency ratio (DFR). The empirical relations between DFR and Ku-band reflectivity have been derived for particles in different regions within the vertical structure of precipitating clouds. The reflectivity conversion using the proposed empirical relations has been tested using real data collected by TRMM-PR and a prototype polarimetric WSR-88D (Weather Surveillance Radar 88 Doppler) radar, KOUN. The processing and analysis of collocated data demonstrate the validity of the proposed empirical relations and substantiate their practical significance for reflectivity conversion, which is essential to the TRMM-based vertical profile of reflectivity correction approach in improving NEXRAD-based QPE.

Citation: Cao, Q.,Y. Hong, Y. Qi, Y. Wen, J. Zhang, J. J. Gourley, and L. Liao (2013), Empirical conversion of the vertical profile of reflectivity from Ku-band to S-band frequency, *J. Geophys. Res. Atmos.*, *118*, 1814–1825, doi:10.1002/jgrd.50138.

1. Introduction

[2] Accurate measurement of precipitation is essential for scientific research in various fields such as meteorology, hydrology, climatology, agriculture, environment, and water resource management. Remote sensing techniques (radar and satellite) have been widely applied as an efficient way to measure precipitation at fine resolution across large regions [*Doviak and Zrnic*, 1993; *Kummerow et al.*, 2000; *Tapiador et al.*, 2012]. As we know, global precipitation measurement has become a major mission of the satellite community [*Tapiador et al.*, 2012]. On the ground, weather radar plays a critical role in measuring storm-scale precipitation. In spite of different resolutions (temporal/spatial) and coverages for precipitation measurement, ground radar and satellite radar can be integrated to achieve more accurate quantitative precipitation estimation (QPE) for various scientific applications.

[3] The U.S. Next-Generation Radar (NEXRAD) network, which consists of 159 S-band (2.8 GHz) WSR-88D (Weather Surveillance Radar 88 Doppler) radars, provides important radar measurements for nationwide weather services. However, the effective coverage of NEXRAD is restricted, especially in the complex terrain of the Intermountain West, leading to insufficient surveillance of low-level atmospheres [*Maddox et al.*, 2002]. It has been realized that QPE based on radar measurements at higher levels can be overestimated or underestimated, depending on whether the radar beam intercepts or overshoots the melting layer [*Gourley and Calvert*, 2003; *Zhang et al.*, 2008]. Much effort has been put into reducing QPE errors through utilizing the vertical profile of reflectivity (VPR) [*Joss and Lee*, 1995; *Fabry and Zawadzki*, 1995; *Vignal*

[1]Advanced Radar Research Center, University of Oklahoma, Norman, Oklahoma, USA.
[2]Hydrometeorology and Remote Sensing Laboratory, National Weather Center, Norman, Oklahoma, USA.
[3]School of Civil Engineering and Environmental Sciences, University of Oklahoma, Norman, Oklahoma, USA.
[4]NOAA/National Severe Storms Laboratory, Norman, Oklahoma, USA.
[5]Goddard Earth Sciences Technology and Research/Morgan State University, Greenbelt, Maryland, USA.

Corresponding author: Y. Hong, Hydrometeorology and Remote Sensing Laboratory and Advanced Radar Research Center, Suite 4610, 120 David L. Boren Blvd., Norman, OK 73072, USA. (yanghong@ou.edu)

2169-897X/13/10.1002/jgrd.50138

et al., 1999; *Matrosov et al*., 2007; *Tabary*, 2007; *Zhang and Qi*, 2010; *Cao et al*., 2012; *Wen et al*., 2012]. Generally, a representative VPR is desirable for the success of VPR-based correction, which becomes problematic in mountainous regions due to beam blockages. Recently, *Cao et al*. [2012] and *Wen et al*. [2012] have proposed the application of spaceborne radar observations to derive necessary VPR information for the correction of ground radar–based QPE. Their studies have taken advantage of the first spaceborne precipitation radar, Tropical Rainfall Measuring Mission's Precipitation Radar (TRMM-PR), which operates at Ku-band with a frequency of 13.8 GHz [*Kozu et al*., 2001]. Compared to horizontally scanning NEXRAD radars, TRMM-PR is much less impacted by mountain blockage and beam broadening effects in the vertical direction [*Kummerow et al*., 2000]. It is capable of providing high-resolution (250 m) observations of the vertical structure of storms. For the ground radar community, the VPR information provided by TRMM-PR is valuable for improving ground radar QPE, especially in complex terrains.

[4] Hydrometeors have different scattering characteristics at different radar frequencies. For a given precipitation system, there may be different VPRs observed by S-band NEXRAD radars and Ku-band TRMM-PR. Therefore, in order to apply TRMM-PR's VPR information in NEXRAD radar QPE, a necessary conversion of VPR from Ku-band to S-band should be considered. *Wen et al*. [2012] have used the physically based VPR model proposed by *Kirstetter et al*. [2010] to fulfill this conversion. However, model errors attributed to the assumptions of icing and melting processes as well as the shape of the VPR have not been fully studied. It is worth noting that many previous studies have provided useful information about the VPR, although they have not directly addressed the particular issue of Ku-band to S-band conversion. Those studies include (1) VPR characteristics and statistics [*Fabry and Zawadzki*, 1995; *Bellon et al*., 2005; *Cao et al*., 2012], (2) the identification of rain, melting layer, and ice regions [*Vignal et al*., 1999; *Gourley and Calvert*, 2003; *Matrosov et al*., 2007; *Boodoo et al*., 2010; *Zhang et al*., 2012; *Qi et al*., 2013, (3) microphysical and scattering models for hydrometeors [*Szyrmer and Zawadzki*, 1999; *Straka and Mansell*, 2005; *Zawadzki et al*., 2005; *Matrosov et al*., 2007; *Ryzhkov et al*., 2011], and (4) dual-frequency (e.g., Ku-band and S-band) properties of hydrometeors [*Liao et al*., 2005; *Liao and Meneghini*, 2009a; *Liao and Meneghini*, 2011; *Grecu et al*., 2011]. Taking advantage of previous findings, the major purpose of this study is to analyze the uncertainty in VPR conversion using theoretical simulations. Through the comparison of Ku-band and S-band reflectivities for different hydrometeors (raindrops, dry/wet snow, and hail), we derive a set of empirical relations for various phases of hydrometeors, which are suitable for the real-time implementation of VPR conversion.

[5] The rest of this paper is organized as follows. Section 2 gives the theoretical basis for this study, including VPR microphysics, radar scattering theory, and the simulation method. Section 3 analyzes the dual-frequency characteristics for 13.8 GHz (Ku-band) of TRMM-PR and 2.8 GHz (S-band) of NEXRAD radar. Empirical relations for the VPR conversion are derived as well. The procedure of VPR conversion from Ku-band to S-band is discussed in section 4 and further illustrated with radar observations. The last section gives conclusions of this work.

2. Theoretical Basis

2.1. Vertical Structure of Precipitation and Radar Observations

[6] Hydrometeors in clouds have a variety of shapes, sizes, orientations, and phases depending on complex microphysical processes (nucleation, icing, growth, melting, evaporation, etc.). Figure 1 shows a schematic of the vertical structure of stratiform precipitation. The VPR can be segregated into three regions according to the phases (solid/liquid) of hydrometeors. Above the freezing level is the ice region, where ice crystals, dry graupel, or snow aggregates normally exist. Below the freezing level, where the temperature is higher than 0°C, the frozen hydrometeors melt until they completely turn into raindrops. This region is generally referred to as the melting layer. As shown in Figure 1, the radar bright band (BB), which is enhanced radar reflectivity attributed to the melting layer, is evident within this region. The existing hydrometeors in the rain region are oblate spheroids. When the freezing level is close to or below the surface, the rain region may not exist and the precipitating particles on the surface will be ice, snow, or a mixture of the two. In strong convection, hail may be observed on the surface because it can grow into large particles aloft and then fall to the ground before completely melting.

[7] Weather radar measures the return signals scattered by hydrometeors in the atmosphere. The equivalent radar reflectivity factor Z_e (hereinafter referred to as the reflectivity) of radar measurement is given by

$$Z_e(\lambda) = \frac{\lambda^4}{\pi^5 |K_w|^2} \int_0^\infty N(D)\sigma_b(D,\lambda)dD, \tag{1}$$

where λ is the radar wavelength, D is the effective particle diameter, $\sigma_b(D,\lambda)$ is the backscattering cross section, and $N(D)$ is the particle size distribution (PSD). The dielectric parameter is $K_w = (\varepsilon_w - 1)/(\varepsilon_w + 2)$, with ε_w being the complex dielectric constant of water. Generally, $|K_w|^2$ has a small variation, approximately 0.91–0.93 for a wavelength of 0.01–0.1 m, and is independent of temperature [*Doviak and Zrnic*, 1993].

2.2. Scattering Model

[8] The scattering characteristics of hydrometeors depend not only on their size, shape, orientation, and composition

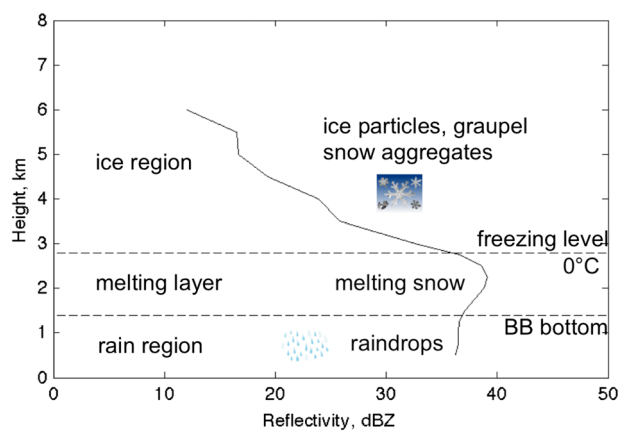

Figure 1. Schematic of ground radar–measured VPR for stratiform precipitation.

but also on wavelength and temperature [*Jung et al.*, 2008; *Ryzhkov et al.*, 2011; *Cao et al.*, 2012]. Scattering models, which are applied to compute the radar variables, need to accommodate these factors. This study considers five different types of hydrometeors, i.e., raindrops, dry snow, dry ice/hail, wet snow, and wet ice/hail. The rest of this subsection addresses the scattering models for these hydrometeors in the following aspects:

[9] 1. Complex dielectric constant: The dielectric constant of air (ε_a) is assumed to be 1, although it has a slight variation depending on the pressure, humidity, and temperature of the atmosphere. The computation of the dielectric constant of water (ε_w) and ice (ε_i) follows that of *Ray* [1972]. The dry/wet snow and ice/hail are mixtures of air, ice, or water, and their densities are determined by the densities of air, ice, and water as well as their composition ratio [*Ryzhkov et al.*, 2011]. Generally, the densities of air, ice, and water are 0.001, 0.917, and 1 g cm^{-3}, respectively. Their composites may have various densities. For example, the density of a dry snow aggregate is normally 0.1–0.6 g cm^{-3}. The density of a wet snow aggregate will increase to 1 g cm^{-3} depending on the melting ratio. Given the composition of air, ice, and water within the hydrometeor, the dielectric constants can be calculated using the Maxwell-Garnett mixing formula [*Ryzhkov et al.*, 2011].

[10] 2. Aspect ratio: Hydrometeors are usually modeled as oblate or prolate spheroids. Considering that raindrops become less spherical and more oblate as their diameters increase, we apply the raindrop size-shape model proposed by *Brandes et al.* [2002] and later verified by *Gourley et al.* [2009]. It is worth noting that the aspect ratio of melting snow and hail has not been as thoroughly investigated. Generally, their aspect ratios vary between 0.6 and 0.9 [*Straka et al.*, 2000]. As suggested by *Jung et al.* [2008], both the snow and ice/hail models used in this study assume a constant aspect ratio of 0.75 and ignore the size variation and melting effect assumed by *Ryzhkov et al.* [2011].

[11] 3. Particle orientation: The amount of backscattered energy received by the radar is related to the scatterer's canting angle with respect to the radar's polarization state. A random Gaussian-distributed canting angle is usually applied for modeling the orientation of hydrometeors. This study assumes a 0° mean canting angle for all types of hydrometeors. The standard deviation (SD) of the canting angle is assumed to be $\sigma = 0°$ for raindrop, $\sigma = 20°$ for snow, and $\sigma = 60°\ (1 - c_w)$ for ice/hail, where c_w is an adjustment parameter and depends on the fractional water content [*Jung et al.*, 2008]. The calculation of radar reflectivity, which considers the effect of the canting angle, follows the formulation reported by *Zhang et al.* [2001] and *Jung et al.* [2008].

[12] 4. Scattering amplitudes: The Rayleigh approximation becomes unsuitable for estimating the scattering of large hydrometeors with diameters that approach the radar wavelength, which is especially the case for Ku-band frequency. The T-matrix method is an efficient numerical technique for computing the scattering amplitude of homogenous, rationally symmetrical, and nonspherical particles [*Vivekanandan et al.*, 1991; *Mishchenko*, 2000]. It is particularly useful for particles that cause Mie scattering, for which the Rayleigh approximation is no longer valid. This study utilizes the modified T-matrix code used by *Cao et al.* [2008, 2012] that includes ice-related hydrometeors. We assume that the particles are uniformly filled for the T-matrix calculation of the hydrometeor's scattering amplitude, as applied in previous studies [*Vivekanandan et al.*, 1991; *Mishchenko*, 2000; *Jung et al.*, 2008], although a two-layer spheroid model for melting snow and ice/hail has been suggested by *Aydin and Zhao* [1990].

2.3. Microphysical Model

[13] The gamma distribution [*Ulbrich*, 1983; *Bringi et al.*, 2002] has been widely used to model the size distribution of hydrometeors. The normalized gamma PSD is given by

$$N(D) = N_w f(\mu)\left(\frac{D}{D_0}\right)^{\mu}\exp(-\Lambda D) \tag{2a}$$

$$\text{with } f(\mu) = \frac{6}{3.67^4}\frac{(3.67+\mu)^{\mu+4}}{\Gamma(\mu+4)}, \text{ and } \Lambda = \frac{3.67+\mu}{D_0}, \tag{2b}$$

where N_w is a normalized concentration parameter, D_0 is the median volume diameter, μ is the shape parameter, Λ is the slope parameter, and Γ is the gamma function. Given the PSD and scattering amplitude (proportional to the backscattering cross section) calculated in section 2.2, the Ku-band and S-band radar reflectivities can be computed for various hydrometeors using equation (1).

3. Analysis

[14] This section focuses on analyzing the dual-frequency characteristics for frequencies of 2.8 GHz (for the S-band NEXRAD radar) and 13.8 GHz (for the Ku-band TRMM-PR). The major purpose of the analysis is to develop empirical relations connecting the two frequencies for VPR conversion in three hydrometeor regions. To better quantify the scattering differences between the two frequencies, we use the radar dual-frequency ratio (DFR), which is defined as follows:

$$\mathrm{DFR} = 10\log_{10}Z_e(\mathrm{S}) - 10\log_{10}Z_e(\mathrm{Ku}), \tag{3}$$

[15] The DFR (in decibels) is independent of the number concentration of particles but depends heavily on the shape and median size of the PSD.

3.1. Rain Region

[16] According to equations (1) and (3) as well as the scattering model assumed in section 2, DFR is uniquely determined by the median volume diameter D_0 given a constant μ for rain PSD. Figure 2a shows the dependence of DFR on D_0 for μ values of −1, 0, 1, 2, 3, and 4. The results are similar to those for 3.0 and 13.8 GHz as reported by *Liao and Meneghini* [2009a]. The DFR is generally negative, except for small values of D_0. The change of DFR is mainly within 2.5 dB for D_0 values less than 3 mm. The DFR varies the most for D_0 values between 0.5 and 2.5 mm. To investigate the variation in DFR, we have assumed a moderate range of parameters for rain PSD or raindrop size distribution (DSD). Similar to *Cao and Zhang* [2009], we have simulated DSDs with μ, D_0, and $\log_{10}(N_w)$ uniformly distributed within the ranges of −1 to 4, 0.5 to 2.5 mm, and 3 to 5, respectively.

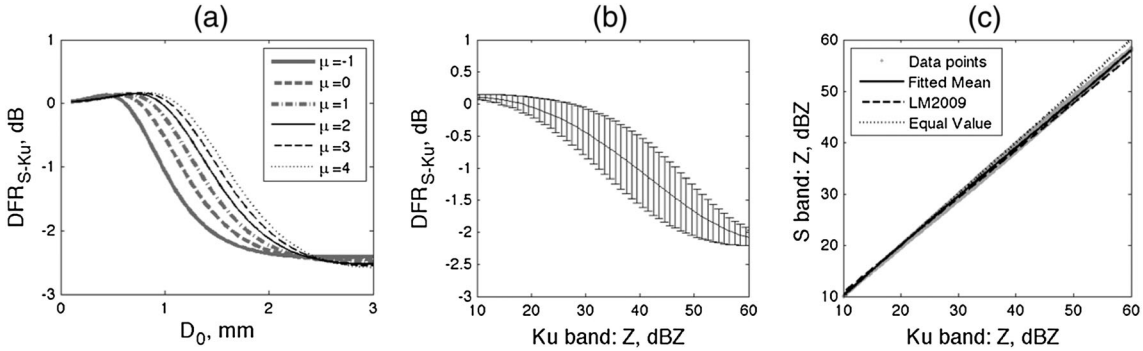

Figure 2. S-band (2.8 GHz) and Ku-band (13.8 GHz) characteristics for rain. (a) Dependence of DFR on D_0 for μ values of -1, 0, 1, 2, 3, and 4. (b) Dependence of DFR on Ku-band reflectivity. The solid line represents the mean relation, whereas the vertical bars denote the SD. (c) Scatter plot of S-band reflectivity vs. Ku-band reflectivity. The solid line is the mean relation fitted to the data points.

Multiyear disdrometer observations in Oklahoma have indicated that the majority of DSDs can be modeled by a gamma distribution using those parameters. Further discussion on the assumption of uniform distribution of DSD (or PSD for snow/hail in the following subsections) parameters is given in section 3.4. Figures 2b and 2c show the statistical results of Ku-band and S-band reflectivities calculated from simulated DSDs. The solid line in Figure 2b indicates the mean curve of DFR in terms of Ku-band reflectivity. It is obtained by fitting a linear regression to all the data points (not shown). The error bars represent the SD of the DFR, which is generally less than 0.5 dB. In addition, the DFR tends to have a relatively larger (or smaller) variation for reflectivities of 35–45 dBZ (or $Z < 25$ dBZ). The dots in Figure 2c denote the data points. The solid line is computed from the fitted mean curve of DFR in Figure 2b. The dashed line represents the Ku-band/S-band relation derived by *Liao and Meneghini* [2009b] (hereinafter referred to as LM2009), which assumes Marshall–Palmer DSD and radar frequencies of 3 and 13.8 GHz, respectively. In spite of these

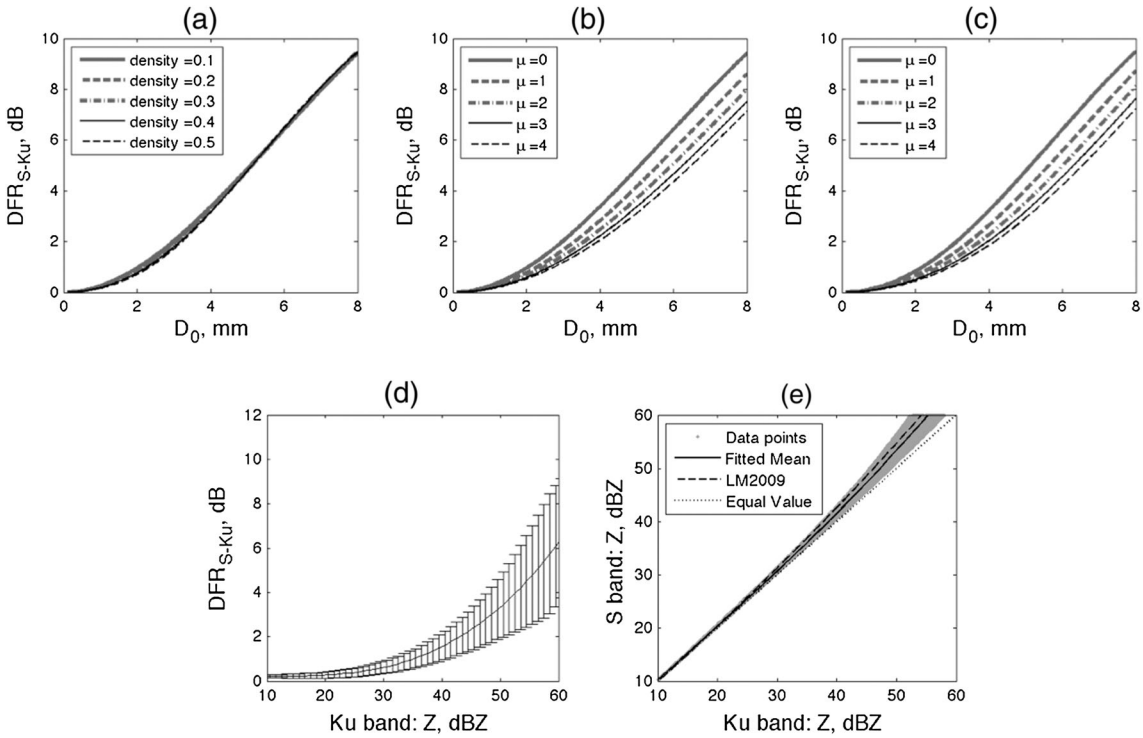

Figure 3. S-band and Ku-band characteristics for dry snow. (a) Dependence of DFR on D_0 for snow densities of 0.1, 0.2, 0.3, 0.4, and 0.5 g cm^{-3}. The value of μ is assumed to 0. (b) Dependence of DFR on D_0 for 0.1 g cm^{-3} of snow density at μ values of 0, 1, 2, 3, and 4. (c) Dependence of DFR on D_0 for 0.3 g cm^{-3} of snow density at μ values of 0, 1, 2, 3, and 4. (d) Same as Figure 2b except for dry snow with a density of 0.3 g cm^{-3}. (e) Same as Figure 2c except for dry snow with a density of 0.3 g cm^{-3}.

differences, LM2009's relation is consistent with the mean curve derived in this study.

3.2. Ice Region

[17] In this region, two types of particles, i.e., dry snow and dry ice/hail particles are studied. Figure 3 shows the dual-frequency characteristics of dry snow particles. Unlike the DFR for rain, the DFR for dry snow is positive and increases with increasing median volume diameter of the PSD. As shown in Figure 3a, the DFR is insensitive to the density of snow particles for a given PSD shape μ. The DFR variation with snow densities, e.g., 0.1 and 0.5 g cm^{-3}, is typically less than 0.3 dB. Figures 3b and 3c compare the DFR for two different snow densities and again illustrate its insensitivity to the snow density. However, they show that the DFR is much more sensitive to the PSD shape. DFR values decrease with increasing PSD shape μ. The DFR difference between the two μ values increases with the median volume diameter. Similar to Figures 2b and 2c, we have simulated PSDs of dry snow with μ, D_0, and $\log_{10}(N_w)$ uniformly distributed within the ranges of 0–2, 0.1–10 mm, and 3–5, respectively. Considering that the DFR is insensitive to snow density, the simulation assumes a constant snow density of 0.3 g cm^{-3}. Figure 3d shows the mean DFR (solid line) in terms of Ku-band reflectivity. The SD of the DFR is less than 0.5 dB for reflectivities less than 45 dBZ. Figure 3e displays the fitted mean S-band/Ku-band relation (solid line) as well as LM2009's dry snow relation (dashed line). Both lines are very similar, with only minor differences attributed to the fact that LM2009's relation assumes the Gunn-Marshall snow PSD, and their DFR is for radar frequencies of 3 vs. 13.8 GHz.

[18] Figure 4 shows the dual-frequency characteristics of dry ice/hail particles. The DFR is also positive and increases monotonically with D_0. It is sensitive to the PSD shape μ as well (Figure 4a). The mean curve of the DFR and S-band reflectivity in terms of Ku-band reflectivity are shown in Figures 4b and 4c, respectively. The μ, D_0, and $\log_{10}(N_w)$ values for the dry ice/hail PSD simulation are in the ranges of 0–2, 0.1–10 mm, and 3–5, respectively. As shown in Figure 4b, the SD of the DFR is also not high, being less than 0.5 dB for reflectivities less than 45 dBZ. Comparing mean DFR curves in Figures 3d and 4b, dry ice/hail particles have smaller DFR values than dry snow particles for a given reflectivity.

3.3. Melting Layer

[19] Snow and ice/hail particles undergoing melting have considerably different dual-frequency characteristics. In the ice region, the DFR is shown to be insensitive to the snow density assumption. However, in the melting layer, the DFR is much more sensitive to it, especially for PSDs with a small D_0. Figure 5a clearly shows the dependence of DFR on the snow density assumption. It is noted that

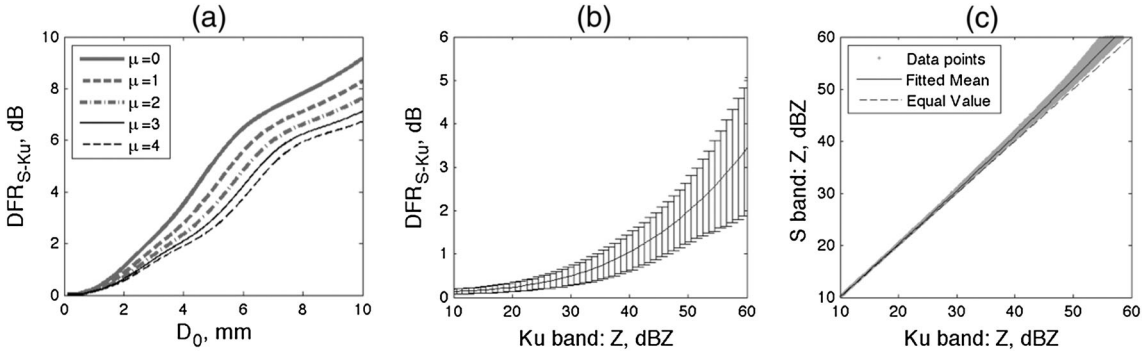

Figure 4. S-band and Ku-band characteristics for dry ice/hail. (a) Dependence of DFR on D_0 for μ values of 0, 1, 2, 3, and 4. (b) Same as Figure 2b except for dry hail. (c) Same as Figure 2c except for dry hail.

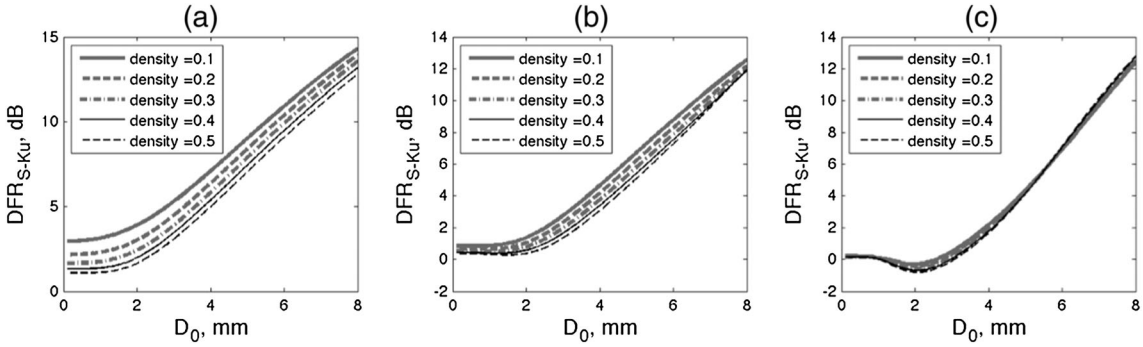

Figure 5. Dependence of DFR on D_0 for melting snow with densities of 0.1, 0.2, 0.3, 0.4, and 0.5 g cm^{-3} and melting ratios of (a) 25%, (b) 50%, and (c) 75%. The μ value is assumed to be 0.

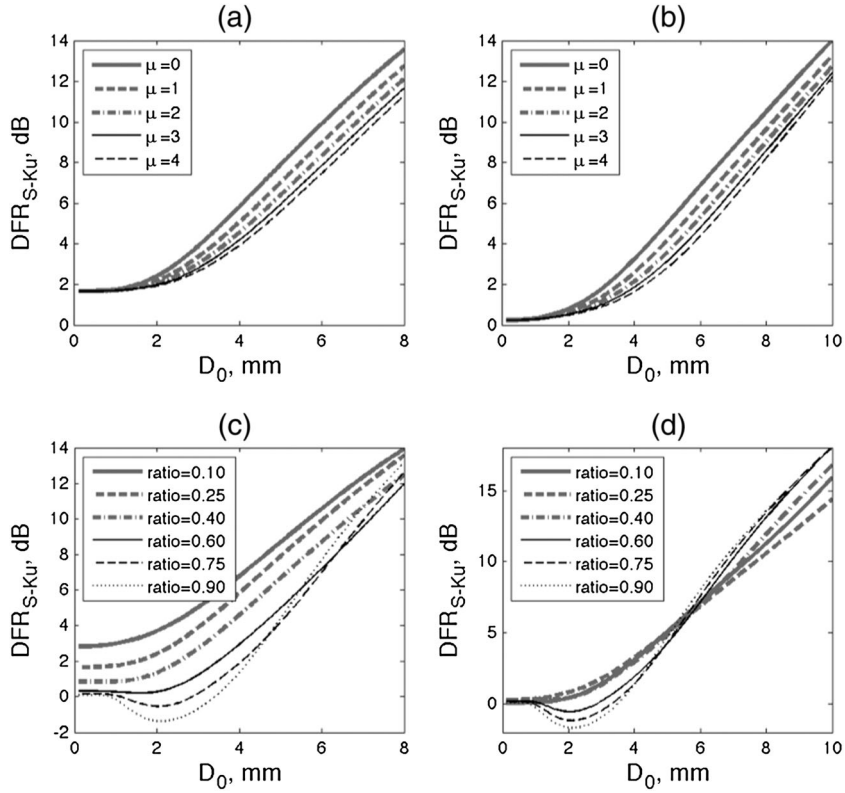

Figure 6. DFR comparison between melting snow (left column) and melting ice/hail (right column) for a melting ratio of 0.25 and μ values of 0, 1, 2, 3, and 4 (a, b) as well as for a μ value of 0 and melting ratios of 0.1, 0.25, 0.40, 0.60, 0.75, and 0.90 (c, d). In Figures 6a and 6c, the snow density is 0.3 g cm^{-3}.

this kind of dependence will decrease with increasing melting ratio, as shown in Figures 5a–5c, with the melting ratio changing from 25% to 75%. Figure 5c presents a very small variation in DFR for different snow densities given a 75% melting ratio.

[20] Figure 6 demonstrates the effects of PSD shape and melting ratio on the DFR and also compares melting snow and ice/hail. As shown in Figures 6a and 6b, with a melting ratio of 0.25, melting snow and ice/hail have similar DFR patterns as follows: (1) the DFR increases with increasing D_0, (2) the PSD shape μ has a similar effect on the DFR, and (3) the DFR has a small variation related to the change in μ when D_0 is less than 2 mm. The difference is that melting snow generally has a larger DFR for a given D_0. As shown in Figures 6c and 6d, the degree of melting affects the DFR of melting snow more than it does that of melting ice/hail. As for snow particles, the melting process normally reduces the DFR for a given PSD, although the DFR may increase with the melting process when the melting ratio exceeds 0.6 and D_0 is large (e.g., >6 mm). Given a large melting ratio, the trend of DFR looks similar between the snow particles and the ice/hail particles. For some PSDs (e.g., D_0 within 1–3 mm), the DFR tends to be negative

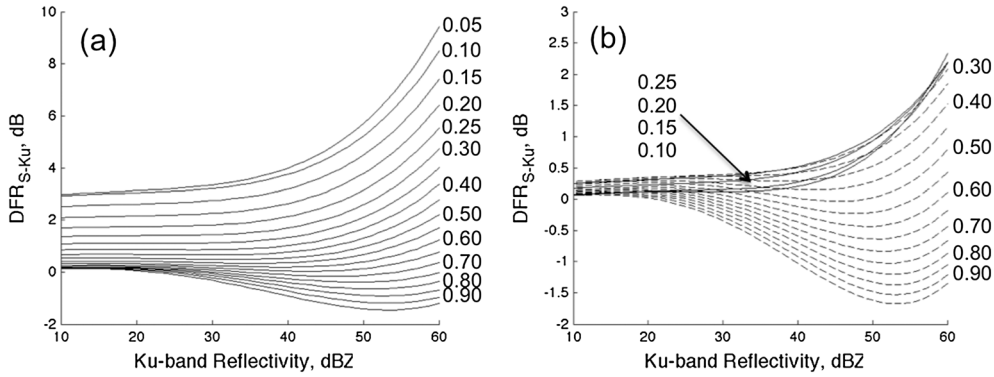

Figure 7. DFR vs. Ku-band reflectivity for different melting ratios. (a) Melting snow with a density of 0.3 g cm^{-3}. (b) Melting hail.

when a large portion of particles are melted. When the melting ratio approaches 100%, the DFR of melting snow tends to approach the DFR of melting ice/snow as well.

[21] To investigate the variation of DFR in the melting layer, the same ranges of parameters shown in Figures 3 and 4 have been applied to simulate the PSDs of melting snow and ice/hail. Although the assumption of snow density could cause some uncertainty in the DFR, especially for cases of partial melting, we have ignored this effect and assumed a constant snow density of $0.3\,\mathrm{g\,cm^{-3}}$. The mean curves of DFR in terms of Ku-band reflectivity are shown in Figure 7 for different melting ratios. It is clearly shown that the melting process introduces a large variation in DFR. All these mean curves, as well as those for rain, dry snow, and ice/hail, are summarized in Table 1 using the following polynomial function:

$$\mathrm{DFR} = a_0 Z_e(\mathrm{Ku})^0 + a_1 Z_e(\mathrm{Ku})^1 + a_2 Z_e(\mathrm{Ku})^2 + a_3 Z_e(\mathrm{Ku})^3 + a_4 Z_e(\mathrm{Ku})^4, \quad (4)$$

where DFR and Z_e(Ku) are expressed in decibels and decibel Z units, respectively. Given these relations, a Ku-band (13.8 GHz) reflectivity can be conveniently converted to an S-band (2.8 GHz) reflectivity for the studied hydrometeor species.

3.4. Error Analysis

[22] The measurements of TRMM-PR can be greatly degraded by precipitation attenuation. Uncertainty may be introduced if the attenuation is not sufficiently corrected. This is one of the major error sources for TRMM-PR–measured reflectivity. The error of Ku-band reflectivity will be propagated into the converted S-band reflectivity. According to equation (4), if the Ku-band error is small, the conversion error can be approximated by

$$\delta_S \approx \delta_{Ku}\left|1 + a_1 + 2a_2 Z_e(\mathrm{Ku}) + 3a_3 Z_e(\mathrm{Ku})^2 + 4a_4 Z_e(\mathrm{Ku})^3\right|, \quad (5)$$

where the notation "| |" denotes the absolute value and δ is the error term (in decibels). As indicated in equation (5), the conversion error δ_S is associated with the Ku-band reflectivity and polynomial coefficients a_1–a_4 listed in Table 1. Fortunately, these coefficients are normally very small and do not have much effect on the total error. With dry snow as an example, given that the Ku-band reflectivity is 50 dBZ and its error δ_{Ku} is 1 dB, the S-band conversion error δ_S is only 1.23 dB.

3.5. Discussion

[23] The derivation of mean DFR curves in previous subsections is based on simulated DSDs/PSDs, whose model parameters have uniform probability distribution functions (PDFs) within certain ranges. Considering that the characteristics of DSDs/PSDs from radar measurements have uncertainty, the assumption of uniform PDFs is reasonable, although additional uncertainty is present in the derived mean DFR curves. Using observed DSDs/PSDs may be a better alternative. However, reliable and ergodic DSDs/PSDs are difficult to obtain, especially for particles aloft. This indicates that observed DSDs/PSDs with biased PDFs may introduce errors in developing the DFR curves. Next, we address the following question: If the true PDF of DSDs/PSDs is not uniformly distributed, do the derived DFR curves change? If the mean values of two PDFs (true vs. uniform) are close, the answer is "No." Figure 8 illustrates the DFR variability attributed to small changes in PSD parameters. The short lines in the figure denote the DFR associated with the change in μ for a given N_w and D_0. It is noted that the DFR typically has a small change (<0.5 dB), with μ varying from 0 to 1, especially for reflectivities less than 45 dBZ. Furthermore, if the change in mean N_w is small (e.g., within 5 dB), then the DFR curves will have only a small difference as well. For example, the DFR curves of dry snow (Figure 8a) have differences not exceeding 0.4, 0.7, and 1 dB for a 5 dB change in N_w given Ku-band reflectivities of 35, 40, and 45 dBZ, respectively. Particularly, the DFR curves for melting snow/

Table 1. Empirical Relations (Coefficients) for Radar Reflectivity Conversion From Ku-band (13.8 GHz) to S-band (2.8 GHz)

Type	DFR (S-Ku) $= a_0 + a_1 \times Z\,(\mathrm{Ku})^1 + a_2 \times Z\,(\mathrm{Ku})^2 + a_3 \times Z\,(\mathrm{Ku})^3 + a_4 \times Z\,(\mathrm{Ku})^4$				
	a_0	a_1	a_2	a_3	a_4
Rain	0.0478	0.0123	-3.504×10^{-4}	-3.30×10^{-5}	4.27×10^{-7}
Dry snow	0.174	0.0135	-1.38×10^{-3}	4.74×10^{-5}	
Dry hail	0.0880	5.39×10^{-2}	-2.99×10^{-4}	1.90×10^{-5}	
10% melting snow	2.82	5.33×10^{-3}	1.005×10^{-3}	-5.78×10^{-5}	1.10×10^{-6}
20% melting snow	2.014	3.34×10^{-3}	8.24×10^{-4}	-5.06×10^{-5}	9.39×10^{-7}
30% melting snow	1.31	2.11×10^{-3}	7.008×10^{-4}	-4.58×10^{-5}	8.22×10^{-7}
40% melting snow	0.816	1.22×10^{-3}	6.13×10^{-4}	-4.15×10^{-5}	7.12×10^{-7}
50% melting snow	0.493	5.96×10^{-4}	5.85×10^{-4}	-3.89×10^{-5}	6.16×10^{-7}
60% melting snow	0.287	5.29×10^{-4}	6.59×10^{-4}	-4.15×10^{-5}	5.80×10^{-7}
70% melting snow	0.159	9.42×10^{-4}	8.16×10^{-4}	-4.97×10^{-5}	6.13×10^{-7}
80% melting snow	0.0812	2.001×10^{-3}	1.035×10^{-3}	-6.44×10^{-5}	7.41×10^{-7}
90% melting snow	0.0412	3.66×10^{-3}	1.17×10^{-3}	-8.08×10^{-5}	9.25×10^{-7}
10% melting hail	0.043	-8.27×10^{-3}	1.66×10^{-3}	-7.19×10^{-5}	9.52×10^{-7}
20% melting hail	0.175	-8.05×10^{-3}	1.21×10^{-3}	-4.66×10^{-5}	6.33×10^{-7}
30% melting hail	0.285	-9.96×10^{-3}	1.45×10^{-3}	-5.33×10^{-5}	6.71×10^{-7}
40% melting hail	0.298	-2.10×10^{-2}	2.44×10^{-3}	-8.56×10^{-5}	9.40×10^{-7}
50% melting hail	0.270	-2.94×10^{-2}	3.22×10^{-3}	-1.12×10^{-4}	1.15×10^{-6}
60% melting hail	0.236	-3.46×10^{-2}	3.71×10^{-3}	-1.30×10^{-4}	1.29×10^{-6}
70% melting hail	0.188	-3.29×10^{-2}	3.75×10^{-3}	-1.39×10^{-4}	1.37×10^{-6}
80% melting hail	0.195	-3.83×10^{-2}	4.14×10^{-3}	-1.54×10^{-4}	1.51×10^{-6}
90% melting hail	0.180	-3.73×10^{-2}	4.08×10^{-3}	-1.59×10^{-4}	1.59×10^{-6}

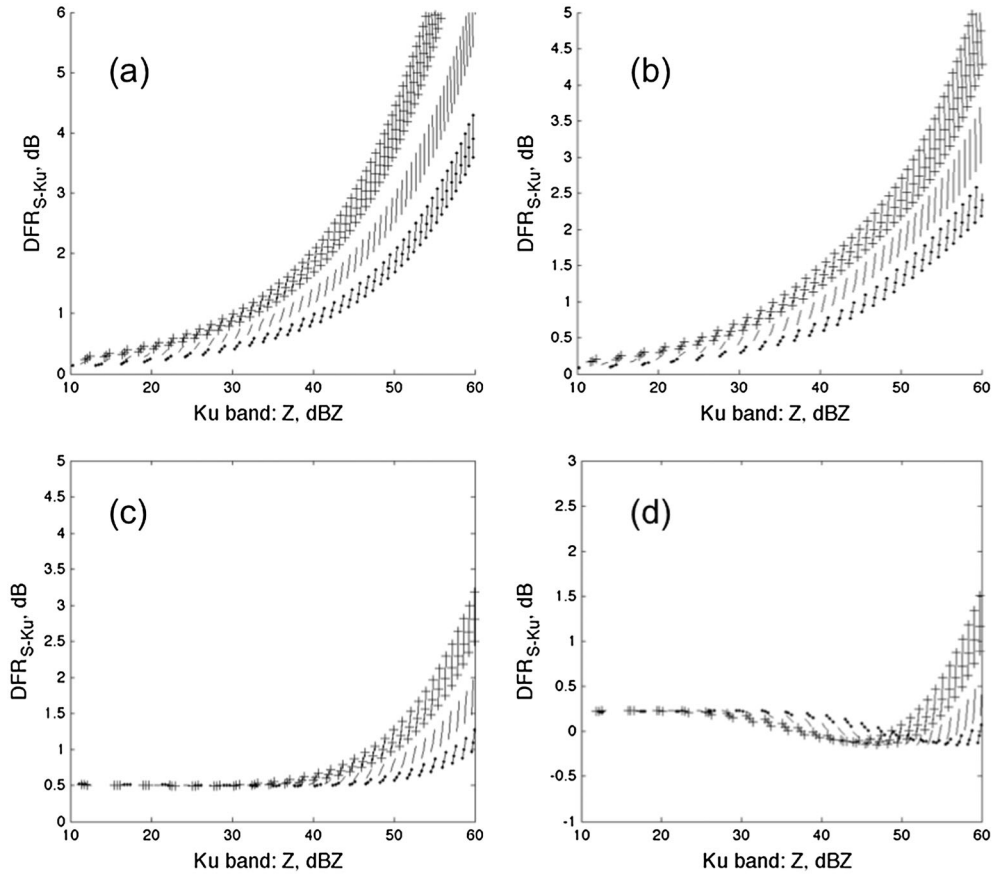

Figure 8. Variability of mean DFR curves caused by the variation in PSD parameters. (a) Dry snow. (b) Dry ice/hail. (c) Melting snow (meting ratio = 0.5). (d) Melting ice/hail (meting ratio = 0.5). The snow density is 0.3 g cm^{-3} in Figures 8a and 8c. Short lines denote the change in μ from 0 to 1, whereas the cross, solid line, and dotted line assume $N_w = 10^{3.5}$, 10^4, and $10^{4.5}$, respectively.

hail particles (as shown in Figures 8c and 8d, with a melting ratio of 50%) are much less sensitive to the change in PSD parameters than those for dry snow/hail particles. This trend is evident for lower reflectivity values (e.g., $Z < 45$ dBZ).

[24] Natural snow/hail PSDs show a large variation in time and space. The simulated PSDs with μ, D_0, and $\log_{10}(N_w)$ uniformly distributed within the ranges of 0–2, 0.1–10 mm, and 3–5, respectively, are expected to represent their major variability. The natural PSDs might have greater variability beyond these ranges. However, according to the aforementioned analysis, the simulated PSDs could derive reasonable mean DFR curves that would be close to those derived from natural PSDs if the mean values of PSD parameters (μ and N_w) vary little. In practice, many previous studies have applied fixed parameters for the snow/hail PSD model, such as the exponential ($\mu = 0$) PSD model [*Jung et al.*, 2008; *Ryzhkov et al.*, 2011]. This kind of assumption would further reduce the variation in DFR. Therefore, we did not apply it in the current study. We are also aware that real microphysical processes could be much more complex than our simulation. However, an in-depth investigation of microphysics is beyond the scope of this study. As Figure 8 suggests, we can tolerate the uncertainty attributed to the microphysical variability, especially for reflectivities less than 45 dBZ. Given the aforementioned discussion, the simulation approach used in this study is reasonable for deriving DFR relations between Ku-bands and S-bands.

4. Application

[25] The derived empirical relations have practical significance for the incorporation of TRMM-PR measurements into NEXRAD-based QPE. Previous studies [e.g., *Tabary*, 2007; *Zhang and Qi*, 2010] have shown that the effect of the BB is a major error source and needs to be corrected for ground radar–based QPE. The approach of TRMM-based VPR correction appears to be a novel solution to this issue for the radar and satellite community [*Wen et al.*, 2012; *Cao et al.*, 2012]. Figure 9 illustrates the procedure of VPR conversion, which is desirable for the purpose of VPR correction. First, the heights of three regions, the ice region, melting layer, and rain region, should be determined prior to DFR conversion. For TRMM-PR, the detection of the BB has been included in the TRMM 2A23 algorithm [*Awaka et al.*, 2009]. Therefore, the relevant TRMM products, such as the boundary of the BB, can be utilized directly. In the ice region, we can choose either the dry snow model or the dry ice/hail model, depending on whether melting snow or melting ice/hail is

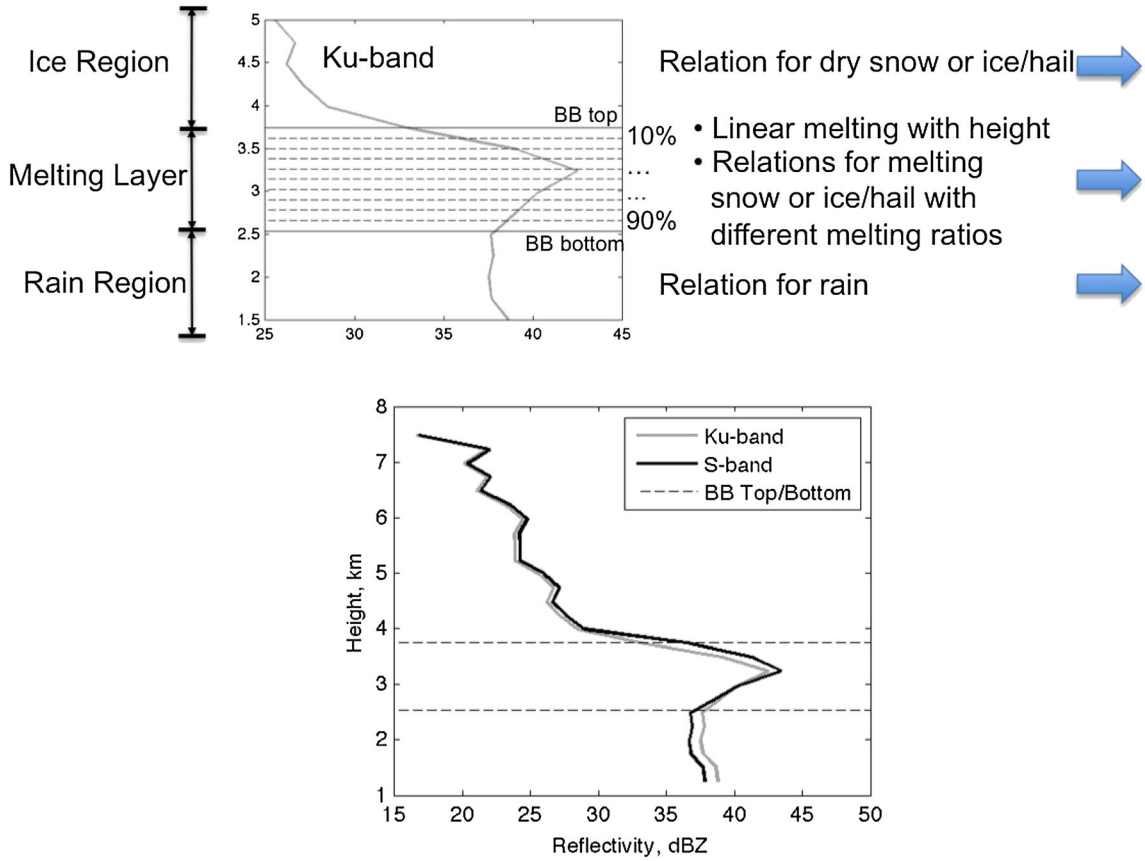

Figure 9. Illustration of VPR conversion from Ku-band to S-band using empirical relations derived in the three regions.

assumed in the melting layer. Although the model choice can be arbitrary, the reflectivity at the freezing level may give some hints; i.e., dry snow particles are likely related to a lower reflectivity (e.g., <35 dBZ) there. The melting process in the melting layer typically involves complicated microphysical processes, which are not fully understood. Accurate modeling of the melting process is beyond the scope of this study. For simplicity, we have assumed that melting is independent of particle size. Furthermore, the melting process is linear, with height changing from top to bottom of the melting layer. This indicates that all particles have the same melting ratio at a given height. As shown in Figure 9, the heights corresponding to the melting ratios of 10%, 20%, . . ., 90% (with 10% intervals) are computed so that the Ku-band VPR can be interpolated to these heights. Based on the empirical relations derived for these melting ratios, the Ku-band reflectivity at these heights is then converted to S-band reflectivity. The conversion is applied to the entire VPR using appropriate relations (Table 1). After the conversion, the S-band VPR can be interpolated onto any height required for such applications as QPE.

[26] The rest of this section incorporates real data to demonstrate the reflectivity conversion. We have utilized the same data sets as those analyzed by *Wen et al*. [2011]. The data sets of 20 events have been collected using KOUN radar, a prototype polarimetric WSR-88D radar located in central Oklahoma, and TRMM-PR. The resolution volume–matching technique has been used for matching data from the KOUN radar and TRMM-PR. The software (available at http://opensource.gsfc.nasa.gov/projects/GPM/index.php) was developed for the global precipitation measurement Ground Validation System Validation Network. The hydrometeor classification algorithm [*Park et al*., 2009] developed by the National Severe Storm Laboratories (NSSL) has been used to identify radar echoes. Details of data sets and data matching have been previously reported [*Wen et al*., 2011]. It is worth noting that the beam broadening effect degrades the radar's vertical resolution at far ranges. In order to minimize these deficiencies, this study has chosen KOUN-PR matched data within 10–50 km from the site of KOUN.

[27] Figure 10 shows the comparison of collocated reflectivity between TRMM-PR and KOUN. Six categories of hydrometeor species have been identified for the comparison. As for the reflectivity conversion, the rain relation in Table 1 is applied to the categories of light or moderate rain and heavy rain. The dry snow relation is applied to the categories of dry snow and graupel. For the categories of wet snow and rain/hail mixture, we have applied the relations of melting snow and melting hail, respectively. The melting ratio has been estimated according to the height of the radar beam relative to the height of the melting layer (TRMM 2A23 products), as suggested in Figure 9. Figure 11 shows the derived PDFs of reflectivity difference (TRMM-PR reflectivity minus KOUN reflectivity). Dashed lines represent comparisons of collocated TRMM-PR and KOUN data prior to correction. The SD values of these distributions are approximately 3 dB, less than the SD values obtained using simulated PSD data (e.g., Figures 2–4). In addition to the frequency difference, there are many other sources contributing to the uncertainty with the matched data.

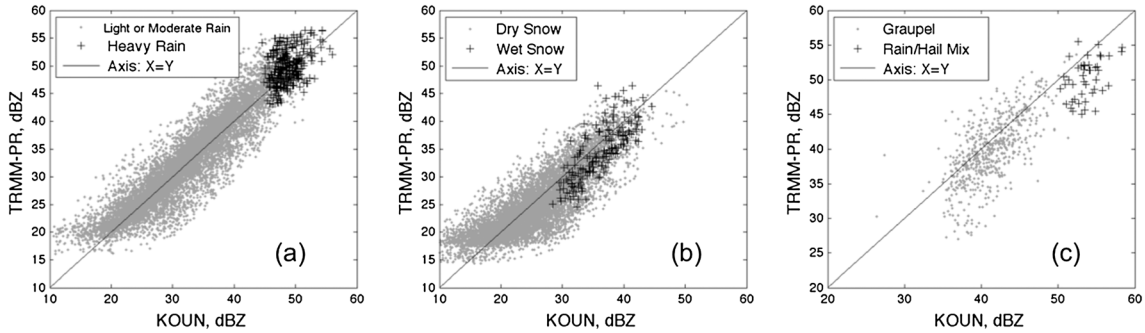

Figure 10. Comparison of TRMM-PR and KOUN reflectivity data for various radar echo classes. (a) Rain. (b) Dry and wet snow. (c) Graupel and rain/hail mixture. The radar data within 10–50 km from the KOUN radar site were applied. The matched data points are 9811, 303, 8702, 174, 608, and 44 for light and moderate rain, heavy rain, dry snow, wet snow, graupel, and rain/hail mixture, respectively.

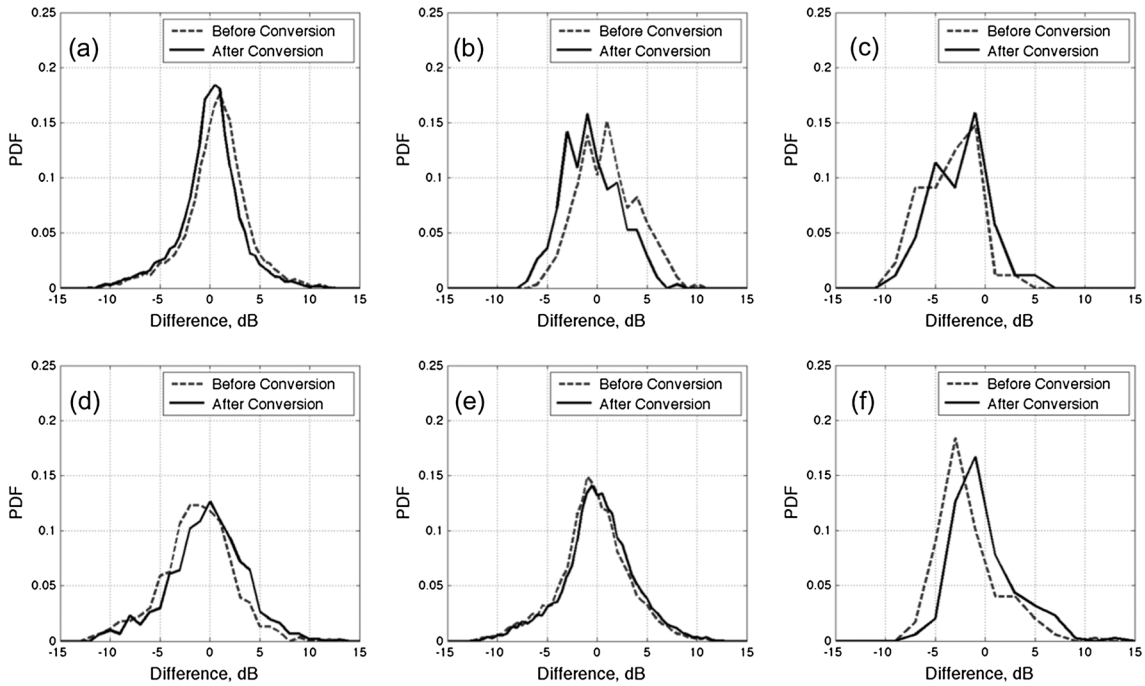

Figure 11. PDFs of reflectivity difference (Ku-band TRMM-PR vs. S-band KOUN) for various radar echo classes. (a) Light or moderate rain. (b) Heavy rain. (c) Rain/hail mixture. (d) Graupel. (e) Dry snow. (f) Wet snow.

One of major sources is the difference in sampling volumes. TRMM-PR generally has a sampling volume with a horizontal (or vertical) dimension of 4.3 km (or 250 m), whereas KOUN has a sampling volume with a dimension of several hundred meters, varying with range and elevation angle. The centers of the sampling volumes are always different as well during data collection. Nevertheless, the data matching process has mitigated this kind of uncertainty as much as possible. TRMM-PR reflectivity data have been converted to S-band and then compared with collocated KOUN data; their differences are

Table 2. Comparison of TRMM-PR and KOUN Reflectivity Data for Various Radar Echo Classes (Before and After Reflectivity Conversion)

	Light or Moderate Rain	Heavy Rain	Dry Snow	Graupel	Rain/Hail Mixture	Wet Snow
Bias (%) (before conversion)	2.07	2.16	−1.47	−3.26	−6.57	−4.95
Bias (%) (after conversion)	0.069	−1.23	0.36	−0.64	−4.75	−0.67

represented by the solid black lines in Figure 11. Although the shapes of the PDFs change little, the mean values shift toward zero, implying that the conversion of reflectivity compensates for the differences attributed to different radar frequencies. The bias values of TRMM-PR and KOUN reflectivity data are listed in Table 2. Ku-band TRMM-PR normally has a higher reflectivity than S-band KOUN for rain categories but has a lower reflectivity for other categories. The reflectivity conversion has effectively reduced the differences between the two radar data sets, demonstrating the ability of the proposed empirical relations to interpret TRMM-PR observations in terms of S-band frequency.

5. Conclusions

[28] This study presents an empirical method for reflectivity conversion from Ku-band (13.8 GHz) to S-band (2.8 GHz) for frozen, mixed-phase, and liquid hydrometeors, which readily facilitates the incorporation of TRMM-PR measurements into NEXRAD-based QPE. The study of dual-frequency reflectivity is based on theoretical simulations, which have assumed appropriate scattering and microphysical models for liquid/solid particles (raindrop, snow, and ice/hail). The dual-frequency characteristics are investigated by simulating various PSDs. Results show that the variation in DFR for rain, dry snow, or dry ice/hail is small (SD is within 0.5 dB) for Ku-band reflectivity values less than 45 dBZ. Compared to the ice/hail hydrometeors, snow particles have a larger variation in DFR, which can be attributed to the melting process. It is therefore necessary to consider the melting process with various melting ratios. We have developed a set of empirical polynomial relations (DFR vs. Ku-band reflectivity) for several hydrometeor species (i.e., dry snow, dry ice/hail, melting snow, melting ice/hail, and raindrops) in different regions of the VPR. The proposed empirical relations have been tested using observations collected by TRMM-PR and KOUN radar. Processing and analysis of collocated data demonstrate that the reflectivity conversion based on the proposed empirical relations effectively reduces the difference attributed to Ku-band and S-band radar frequencies.

[29] Recently, the study of improving NEXRAD-based QPE by incorporating observations from TRMM-PR has attracted research interests in the radar and satellite communities. For example, the VPR correction method based on TRMM-PR observations has been introduced to mitigate the effects of radar melting layer observations on ground radar QPE. The derived DFR relations in this study can be directly applied to convert TRMM-PR reflectivity to the frequency of NEXRAD. Therefore, they have practical significance for combining TRMM-PR with NEXRAD for the improvement of ground radar QPE, especially for stratiform precipitation. Overall, this study contributes to the synergistic development of QPE algorithms using radar observations from space and ground. Future work will include Ka-band radar observations in preparation for the upcoming global precipitation measurement mission.

[30] **Acknowledgments.** This work was partially supported by NASA grant NNX11AL78G under the "Incorporating NASA Spaceborne Precipitation Research Products into National Mosaic QPE Real-time System for Improved Short-term Weather Prediction at Colorado Basin River Forecast Center" label. We appreciate the support from NSSL personnel who made the KOUN radar data available. We are also thankful for the support from NASA TRMM for providing the PR data, which are archived and distributed by the Goddard Earth Sciences Data and Information Services Center.

References

Awaka, J., T. Iguchi, and K. Okamoto (2009), TRMM PR standard algorithm 2A23 and its performance on bright band detection, *J. Meteorol. Soc. Jpn. 87A*, 31–52.

Aydin, K., and Y. Zhao (1990), A computational study of polarimetric radar observables in hail, *Geoscience and Remote Sensing, IEEE Transactions on*, *28*, 4, 412–422.

Bellon, A., G. W. Lee, and I. Zawadzki (2005), Error Statistics of VPR Corrections in Stratiform Precipitation, *J. Appl. Meteor.*, *44*, 998–1015.

Boodoo, S., D. Hudak, N. Donaldson, M. Leduc (2010), Application of dual-polarization radar melting-layer detection algorithm, *J. Appl. Meteor. Climatol.*, *49*, 1779–1793.

Brandes, E.A., G. Zhang, J. Vivekanandan (2002), Experiments in rainfall estimation with a polarimetric radar in a subtropical environment, *J. Appl. Meteor.*, *41*, 674–685.

Bringi, V.N., G. Huang, V. Chandrasekar, and E. Gorgucci (2002), A Methodology for Estimating the Parameters of a Gamma Raindrop Size Distribution Model from Polarimetric Radar Data: Application to a Squall-Line Event from the TRMM/Brazil Campaign, *J. Atmos. Oceanic Technol.*, *19*, 633–645.

Cao, Q., G. Zhang, E. Brandes, T. Schuur, A. Ryzhkov, and K. Ikeda (2008), Analysis of Video Disdrometer and Polarimetric Radar Data to Characterize Rain Microphysics in Oklahoma, *J. Appl. Meteor. Climatol.*, *47*, 2238–2255.

Cao, Q., and G. Zhang (2009), Errors in estimating raindrop size distribution parameters employing disdrometer and simulated raindrop spectra, *J. Appl. Meteor. Climatol.*, *48*, 406–425.

Cao, Q., Y. Hong, and co-authors (2012), Statistical and Physical Analysis of Vertical Structure of Precipitation in Mountainous West Region of US using 11+ Year Spaceborne TRMM PR Observations, *J. Appl. Meteor. Climatol.*, doi:http://dx.doi.org/10.1175/JAMC-D-12-095.1.

Doviak, R., and D. Zrnic (1993), Doppler Radar and Weather Observations, 2nd ed., San Diego, CA: Academic, 1993.

Fabry, F., and I. Zawadzki (1995), Long-Term Radar Observations of the Melting Layer of Precipitation and Their Interpretation, *J. Atmos. Sci.*, *52*, 838–851.

Gourley, J. J., and C. M. Calvert (2003), Automated Detection of the Bright Band Using WSR-88D Data. *Wea. Forecasting*, *18*, 585–599.

Gourley, J. J., A. J. Illingworth, and P. Tabary (2009), Absolute calibration of radar reflectivity using redundancy of the polarization observations and implied constraints on drop shapes, *J. Atmo. and Ocean. Tech.*, *26*, 689–703.

Grecu, M., L. Tian, W. S. Olson, and S. Tanelli (2011), A Robust Dual-Frequency Radar Profiling Algorithm, *J. Appl. Meteor. Climatol.*, *50*, 1543–1557.

Joss, J., and R. Lee (1995), The Application of Radar-Gauge Comparisons to Operational Precipitation Profile Corrections, *J. Appl. Meteor.*, *34*, 2612–2630.

Jung, Y., G. Zhang, and M. Xue (2008), Assimilation of simulated polarimetric radar data for a convective storm using the ensemble Kalman filter. Part I: observation operators for reflectivity and polarimetric variables, *Mon. Wea. Rev.*, *136*, 2228–2245.

Kirstetter, P., H. Andrieu, G. Delrieu, and B. Boudevillain (2010), Identification of Vertical Profiles of Reflectivity for Correction of Volumetric Radar Data Using Rainfall Classification, *J. Appl. Meteor. Climatol.*, *49*, 2167–2180.

Kozu, T., and Co-authors (2001), Development of precipitation radar onboard the Tropical Rainfall Measuring Mission (TRMM) satellite, *Geoscience and Remote Sensing, IEEE Transactions on*, *39*, 1, 102–116, Jan 2001, doi: 10.1109/36.898669.

Kummerow, C., and Coauthors (2000), The Status of the Tropical Rainfall Measuring Mission (TRMM) after Two Years in Orbit, *J. Appl. Meteor.*, *39*, 1965–1982.

Liao, L., R. Meneghini, T. Iguchi, and A. Detwiler (2005), Use of Dual-Wavelength Radar for Snow Parameter Estimates, *J. Atmos. Oceanic Technol.*, *22*, 1494–1506.

Liao, L., and R. Meneghini (2009a), Validation of TRMM Precipitation Radar through Comparison of Its Multiyear Measurements with Ground-Based Radar, *J. Appl. Meteor. Climatol.*, *48*, 804–817.

Liao, L., and R. Meneghini (2009b), Changes in the TRMM Version-5 and Version-6 Precipitation Radar Products Due to Orbit Boost, *J Meteorol Soc Jpn.* 2009, *87* (Sp. Iss. SI), 93–107.

Liao, L., and R. Meneghini (2011), A Study on the Feasibility of Dual-Wavelength Radar for Identification of Hydrometeor Phases, *J. Appl. Meteor. Climatol.*, *50*, 449–456.

Maddox, R. A., J. Zhang, J. J. Gourley, and K. W. Howard (2002), Weather Radar Coverage over the Contiguous United States, *Wea. Forecasting*, *17*, 927–934.

Matrosov, S. Y., K. A. Clark, and D. E. Kingsmill (2007), A Polarimetric Radar Approach to Identify Rain, Melting-Layer, and Snow Regions for Applying Corrections to Vertical Profiles of Reflectivity, *J. Appl. Meteor. Climatol.*, *46*, 154–166.

Mishchenko, M. I. (2000), Calculation of the Amplitude Matrix for a Nonspherical Particle in a Fixed Orientation, *Appl. Optics*, *39*, 6, 1026–1031.

Park, H. S., A. V. Ryzhkov, D. S. Zrnić, and K.-E. Kim (2009), The Hydrometeor Classification Algorithm for the Polarimetric WSR-88D: Description and Application to an MCS, *Wea. Forecasting*, *24*, 730–748.

Qi, Y., J. Zhang, and P. Zhang (2013), A Real-time Automated Convective And Stratiform Precipitation Segregation Algorithm in Native Radar Coordinates, *Q. J. R. Meteorol. Soc.*, doi:10.1002/qj.2095.

Ray, P. (1972), Broadband complex refractive indices of ice and water, *Appl. Opt.*, *11*, 1836–1844.

Ryzhkov, A., M. Pinsky, A. Pokrovsky, and A. Khain (2011), Polarimetric Radar Observation Operator for a Cloud Model with Spectral Microphysics, *J. Appl. Meteor. Climatol.*, *50*, 873–894.

Straka, J. M., D. S. Zrnić, and A. V. Ryzhkov (2000), Bulk Hydrometeor Classification and Quantification Using Polarimetric Radar Data: Synthesis of Relations, *J. Appl. Meteor.*, *39*, 1341–1372.

Straka, J. M., and E. R. Mansell (2005), A Bulk Microphysics Parameterization with Multiple Ice Precipitation Categories, *J. Appl. Meteor.*, *44*, 445–466.

Szyrmer, W., and I. Zawadzki (1999), Modeling of the Melting Layer. Part I: Dynamics and Microphysics, *J. Atmos. Sci.*, *56*, 3573–3592.

Tabary, P. (2007), The New French Operational Radar Rainfall Product. Part I: Methodology, *Wea. Forecasting*, *22*, 393–408.

Tapiador, F. J., F. J. Turk and co-authors (2012), Global precipitation measurement: Methods, datasets and applications, *Atmos. Res.*, *104–105*, February 2012, Pages 70-97, ISSN 0169-8095, 10.1016/j.atmosres.2011.10.021.

Ulbrich, C. W. (1983), Natural variations in the analytical form of the raindrop size distribution, *J. Climate Appl. Meteorol.*, *22*, 1764–1775.

Vignal, B., H. Andrieu, and J. Dominique Creutin (1999), Identification of vertical profiles of reflectivity from volume scan radar data, *J. Appl. Meteor.*, *38*, 1214–1228.

Vivekanandan, J., W. M. Adams, and V. N. Bringi (1991), Rigorous Approach to Polarimetric Radar Modeling of Hydrometeor Orientation Distributions, *J. Appl. Meteor.*, *30*, 1053–1063.

Wen, Y., Y. Hong, and co-authors (2011), Cross validation of spaceborne radar and ground polarimetric radar aided by polarimetric echo classification of hydrometeor types, *J. Appl. Meteor. Climatol.*, *50*, 1389–1402.

Wen, Y., Q. Cao, and co-authors (2012), Incorporating NASA space-borne radar data into NOAA National Mosaic QPE system for improved precipitation measurement: a physically based VPR identification and enhancement method, *Journal of Hydrometeorology*, in minor revision after peer-review.

Zawadzki, I., W. Szyrmer, C. Bell, and F. Fabry (2005), Modeling of the Melting Layer. Part III: The Density Effect, *J. Atmos. Sci.*, *62*, 3705–3723.

Zhang, G., J. Vivekanandan, and E. A. Brandes (2001), A method for estimating rain rate and drop size distribution from polarimetric radar, *IEEE Trans. Geosci. Remote Sens.*, *39*, 4, 830–840.

Zhang, J., and Y. Qi (2010), A Real-Time Algorithm for the Correction of Brightband Effects in Radar-Derived QPE, *J. Hydrometeor*, *11*, 1157–1171.

Zhang, J., Y. Qi, D. Kingsmill, and K. Howard (2012), Radar-based quantitative precipitation estimation for the cool season in complex terrain: case studies from the NOAA hydrometeorology Testbed, *J. Hydrometeor.* doi:10.1175/JHM-D-11-0145.1, in press.

Zhang, J., C. Langston, and K. Howard (2008), Brightband identification based on vertical profiles of reflectivity from the WSR-88D, *J. Atmos. Oceanic Technol.*, *25*, 1859–1872.